Production mechanism of neutron-rich nuclei around $N=126$ in the multi-nucleon transfer reaction ^{132}Sn + ^{208}Pb*

Xiang Jiang(蒋翔) Nan Wang(王楠)[1)]

College of Physics and Energy, Shenzhen University, Shenzhen 518060, China

Abstract: The time-dependent Hartree-Fock approach in three dimensions is employed to study the multi-nucleon transfer reaction ^{132}Sn + ^{208}Pb at various incident energies above the Coulomb barrier. Probabilities for different transfer channels are calculated by using the particle-number projection method. The results indicate that neutron stripping (transfer from the projectile to the target) and proton pick-up (transfer from the target to the projectile) are favored. De-excitation of the primary fragments is treated by using the state-of-art statistical code GEMINI++. Primary and final production cross sections of the target-like fragments (with $Z=77$ to $Z=87$) are investigated. The results reveal that fission decay of heavy nuclei plays an important role in the de-excitation process of nuclei with $Z>82$. It is also found that the final production cross sections of neutron-rich nuclei depend only slightly on the incident energy, while those of neutron-deficient nuclei depend strongly on the incident energy.

Keywords: transfer reaction, neutron-rich nuclei, time-dependent Hartree-Fock approach, particle-number projection method, GEMINI++, evaporation residuals

PACS: 25.70.Hi, 24.10.-i **DOI:** 10.1088/1674-1137/42/10/104105

1 Introduction

Neutron-rich nuclei, especially those far from the β-stability line, are very important to study nuclear structure, elucidate reaction mechanisms and provide information on the astrophysical r process, which is responsible for the synthesis of half of the naturally occurring nuclei heavier than iron [1]. Neutron-rich nuclei can also be used as projectiles to synthesize super-heavy nuclei located at the island of stability, which is one of the goals of present and future radioactive ion beam facilities.

Neutron-rich nuclei in the region of $N=126$ (the last waiting point along the r process) can help to understand the alteration of the shell gap in the presence of the neutron excess [2] and the observed peak structure around $A\sim195$ in the solar r-abundance distribution [3]. However, due to the difficulties in producing, detecting and identifying these nuclei in experiments, there are few relevant investigations on them. Recently, multi-nucleon transfer (MNT) reactions in the vicinity of the Coulomb barrier have been shown to be a feasible route to populate these heavy neutron-rich nuclei. Recent theoretical [4–8] and experimental [2, 3, 9, 10] results indicate that much larger cross sections can be obtained in MNT reactions than in projectile fragmentations (the main method to produce neutron-rich nuclei with moderate mass). Nevertheless, large-scale experiments are not practical due to the difficulties mentioned above. Therefore, reliable theoretical predictions of probable projectile-target combinations, incident energies and so on can help to guide relevant experiments.

For this purpose, various models have been established in recent years. For example, Langevin type equations of motion [4–6], the semiclassic GRAZING model [11, 12], the dinuclear system (DNS) model [7, 13, 14] and the improved quantum molecular dynamics (ImQMD) model [8, 15–17] have been successful in measurements of MNT in asymmetric reactions. However, in low-energy reactions around the Coulomb barrier, nuclear structure and quantum effects play very important roles. Therefore, it is desirable to describe the reactions in nucleonic degrees of freedom quantum mechanically and without adjustable parameters.

The time-dependent Hartree-Fock (TDHF) approach provides a good approximation for microscopically describing the dynamics of such quantum many-body systems at low energies [18]. It was first proposed by Dirac in 1930 [19]. Present-day three-dimensional (3D) TDHF calculations with modern Skyrme parametrizations are applied to low-energy heavy-ion collisions in many subjects, for instance, collective vibration [20–23], fusion reactions [24–27], fission dynamics [28–30], dissipation

Received 10 July 2018, Published online 27 August 2018

∗ Supported by National Natural Science Foundation of China (11705118, 11475115, 11647026) and Natural Science Foundation of SZU (2016017)

1) E-mail: wangnan@szu.edu.cn, Corresponding author

mechanisms [31–37], transfer reactions [15, 38], and so on. Recently, with the help of the particle-number projection (PNP) method [18, 39], the probabilities for different transfer channels can be obtained. To compare with experimental data, de-excitation of hot primary fragments should be considered. However, this is one of the drawbacks of dynamical models such as TDHF and ImQMD. One reason is that the timescale of the de-excitation process ($\sim 10^{-17}$ s) is much longer than that of the dynamical collisions. This can be cured by using the statistical code GEMINI++ after dynamical simulations. Such a combination has been widely used recently [8, 38, 40–42].

This paper is organized as follows. An outline of the TDHF+GEMINI method and numerical details are given in Section 2. Simulation results are presented and discussed in Section 3. Finally, a summary is given in Section 4.

2 Formalism and numerical details

2.1 TDHF approach and PNP method

The single-particle wave functions in the TDHF approach satisfy the fully microscopic equations

$$\mathrm{i}\hbar\partial_t\psi_\alpha = \hat{h}[\rho]\psi_\alpha, \tag{1}$$

which can be derived from a variational principle [43], where $\hat{h}$ is the self-consistent mean-field Hamiltonian of single-particle motion and is related to the Skyrme functionals, and ρ is the one-body density matrix of the independent particle system. The state of the whole system Ψ is preserved as a Slater determinant, which is an anti-symmetrized product of all single-particle wave functions.

In TDHF collisions, nucleons can be exchanged between the reactants once they have contact with each other. Single-particle wave functions are partially transfered from the projectile to the target and vice versa. The average proton and neutron numbers of the fragments can be obtained as expectation values of the particle number operators $\hat{N}^p$ (for protons) and $\hat{N}^n$ (for neutrons) as $\langle\Psi|\hat{N}^q|\Psi\rangle$ $(q=p,n)$. However, the TDHF states are not eigenstates of the particle number operators but superpositions of these eigenstates. The many-body states can be projected on good particle numbers (N protons or neutrons) by introducing PNP operator, expressed as integrals over gauge angles in subspace V [18, 39]

$$\hat{P}_{N;V} = \frac{1}{2\pi}\int_0^{2\pi} \mathrm{d}\theta \mathrm{e}^{\mathrm{i}\theta(\hat{N}_V - N)}, \tag{2}$$

where $\hat{N}_V = \sum_{\alpha=1}^{N^q_{\rm tot}} \Theta_V(\boldsymbol{r})$ and $\Theta_V(\boldsymbol{r}) = 1$ if $\boldsymbol{r} \in V$ and 0 elsewhere. $N^q_{\rm tot}$ is the total states of nucleons with isospin q.

At a given incident energy, Eq. (2) can be used to compute the probability $P_{N;V}(b)$ of finding N particles in space V for each impact parameter b. For later discussion, $P_{N;V}(b)$ is replaced by $P_N(b)$ for simplicity. The production cross section of a primary fragment composed of N neutrons and Z protons at a certain incident energy is

$$\sigma_{N,Z} = 2\pi\int_{b_{\rm min}}^{b_{\rm max}} b\mathrm{d}bP_{N,Z}(b), \tag{3}$$

where $P_{N,Z}(b) = P_N(b)P_Z(b)$, $b_{\rm min}$ is the critical impact parameter inside which fusion happens. In this work, $b_{\rm min}=0$ is used for all incident energies because only binary products are found for all impact parameters. $b_{\rm max}$ is a cutoff impact parameter which depends on the incident energy and will be given later. Note that $b_{\rm max}$ should be large enough to make sure that transfer cross sections barely depend on the choice of it.

2.2 De-excitation after collisions

The state-of-art statistical code GEMINI++ is used to treat the de-excitation process of the hot primary fragments produced in TDHF collisions. This code is an improved version of GEMINI, which is based on the well-known sequential-binary-decay picture where the individual compound nuclei decay through sequential binary decays of all possible modes (evaporation of neutron, emission of light charged particles, symmetric and asymmetric fission of heavy nuclei), until the resulting products are unable to undergo any further binary decay due to competition with γ-ray emission [44]. The decay width for the evaporation of fragments with $Z\leqslant 2$ is calculated using the Hauser-Feshbach formalism [45]. The transmission coefficient and the level-density parameter are improved in GEMINI++. The fission decay width is calculated using Moretto's transition state formalism for a light system or asymmetric fission of a heavy system. The Bohr-Wheeler formalism is used in conjunction with the systematics of mass distribution for more symmetric fission of a heavy system [46]. Furthermore, extensive comparisons with heavy-ion induced fusion data have been used to optimize the default parameters for GEMINI++. Further details can be found in Refs. [44, 46] and references therein. The original version of GEMINI++ with default parameters is used in the present work [47, 48].

For a certain primary fragment with (N',Z'), excitation energy $E^*_{N',Z'}$ and angular momentum $J_{N',Z'}$ (these quantities will be given in the following subsection), the de-excitation process of this fragment should be repeated $M_{\rm trial}$ times due to the statistical nature of GEMINI++. After de-excitation, the number of events in which a final fragment with (N,Z) occurs is counted and denoted as $M_{N,Z}$. Then the production cross section of the final

fragment with (N,Z) is given as

$$\sigma_{N,Z}^{\rm final}=2\pi\int_{b_{\rm min}}^{b_{\rm max}} b{\rm d}b \sum_{N'\geqslant N,Z'\geqslant Z} P_{N',Z'}(b)\frac{M_{N,Z}}{M_{\rm trial}}. \quad (4)$$

2.3 Numerical details

In the present work, the 3D unrestricted TDHF code Sky3D [49] is used to compute the collisions. The Skyrme SLy6 parametrization [50] is adopted for the static and dynamic calculations. The initial nuclei are prepared by the static HF using the damped gradient iteration [51] with the imaginary time-step method [52]. The static iterations are performed on $32\times32\times32$ Cartesian grids with 1.0 fm grid spacing in all three directions.

In the dynamical calculations, the meshes are extended to 70×32×70 while the grid spacing is kept constant as in static HF. The two nuclei are initially placed at a separation distance of 24 fm between their mass centers along the z-axis. They are boosted with velocities obtained assuming that they move on a pure Rutherford trajectory with the associated center-of-mass (c.m.) energy $E_{\rm c.m.}$ at infinite distance until they reach the initial separation distance. Equation (1) is solved iteratively with a time step $\triangle t$=0.2 fm/c and the exponential propagator is replaced by a Taylor series expansion up to order 6. All the reactions are simulated until the separation distance between the primary fragments' mass centers reaches 30 fm.

In PNP analysis, the integrals over θ in Eq. (2) are performed with an $M-$point uniform discreteness. M=300 is adopted for convergence.

To deal with the de-excitation process, the mass and charge numbers, excitation energy and angular momentum of the primary fragment should be provided as inputs of GEMINI++. For a certain transfer channel with N neutrons and Z protons in the target-like fragment (TLF), and $N_{\rm tot}-N$ neutrons and $Z_{\rm tot}-Z$ protons in the projectile-like fragment (PLF), the mass and charge numbers of the TLF are $N+Z$ and Z, respectively. The total excitation energy of the system at final distance is taken to be $E^*_{\rm tot}=E_{\rm c.m.}-{\rm TKE}+Q_{gg}(N,Z)$, where TKE represents the total kinetic energy of the primary fragments and Q_{gg} is the reaction Q value. The ground-state masses are taken from AME2016 [53, 54] and FRDM(2012) [55] to calculate the Q value for each transfer channel. $E^*_{\rm tot}$ is shared between the outgoing fragments in proportion to their masses. The average angular momentum of the fragments can be directly obtained in TDHF. The number of trial events $M_{\rm trial}$ in GEMINI++ is set as 1000.

3 Results and discussion

3.1 Overview of the TDHF results

In this subsection, the TDHF results of ^{132}Sn + ^{208}Pb without de-excitation are presented. This reaction is one of the candidates for producing heavy neutron-rich nuclei around $N=126$. The simulations are performed at three incident energies, 470, 550 and 800 MeV, in the c.m. frame. These are about 1.2, 1.4 and 2 times the Bass barrier (∼400 MeV). For each bombarding energy, the impact parameter ranges from 0 to $b_{\rm max}$ ($b_{\rm max}$=10 fm, 12 fm and 13 fm for the three energies) with the interval Δb=1 fm.

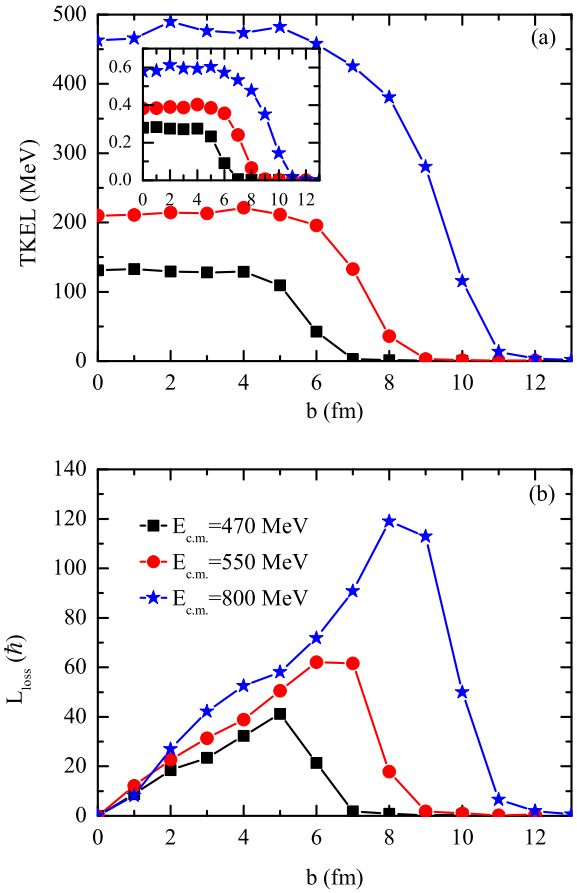

Fig. 1. (color online) (a) Total kinetic energy loss and (b) orbital angular momentum loss as functions of the impact parameter for ^{132}Sn + ^{208}Pb at $E_{\rm c.m.}$=470 MeV (black squares), 550 MeV (red circles) and 800 MeV (blue stars). TKEL/$E_{\rm c.m.}$ as a function of the impact parameter for the three incident energies are shown in the inset of the upper panel. The lines are drawn to guide the eye.

Shown in Fig. 1 are the total kinetic energy loss (TKEL) and orbital angular momentum loss ($L_{\rm loss}$) as functions of the impact parameter. TKEL is defined as $E_{\rm c.m.}-$TKE. $L_{\rm loss}$ is taken to be the difference in initial and final orbital angular momenta. It can be found in Fig. 1(a) that the TKEL shows a smooth dependence on the impact parameter. A plateau pattern can be seen up to b=5 fm for all the three energies, and then TKEL decreases gradually with the increasing impact parameter.

Strong energy dependence of TKEL and TKEL/$E_{c.m.}$ is observed in Fig. 1(a) and the inset. They both increase with increasing incident energy. This is due to the fact that more nucleons are exchanged between the projectile and the target nuclei at higher energies. As a consequence, the collisions become more violent and more energies of collective motion should be dissipated. We note in Fig. 1(b) that L_{loss} increases linearly with the impact parameter up to b=5, 7 and 8 fm for the three incident energies, respectively. At larger impact parameters, it decreases gradually as expected. Energy dependence is also observed for L_{loss}.

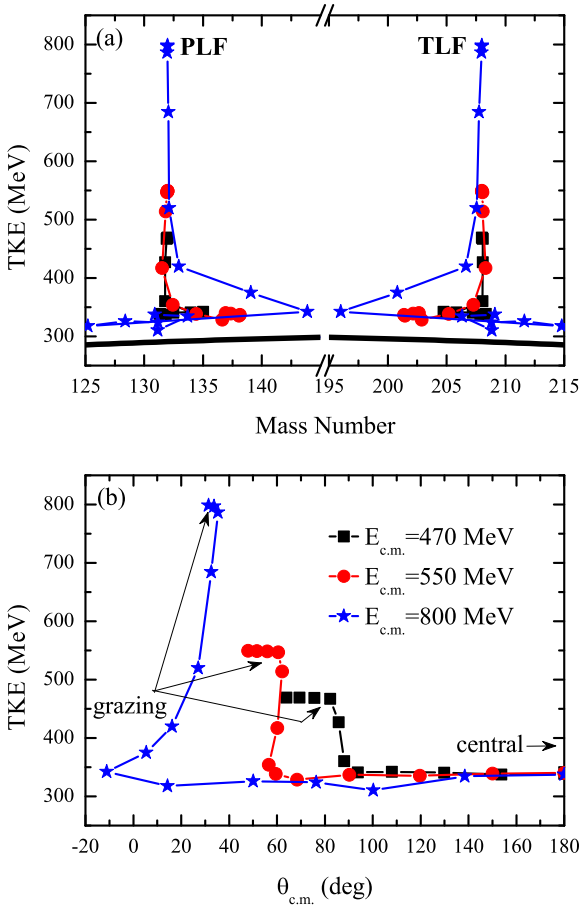

Fig. 2. (color online) Total kinetic energy of the outgoing fragments versus (a) mass of the primary fragment and (b) scattering angle in the c.m. frame for ^{132}Sn + ^{208}Pb at $E_{c.m.}$=470 MeV (black squares), 550 MeV (red circles) and 800 MeV (blue stars). TKEs deduced from Viola systematics are shown in the upper panel as a thick solid line for comparison.

Figure 2(a) shows TKE as a function of the masses of the primary fragments. The results of Viola systematics [56, 57] (the relative momentum in the entrance channel is fully damped and TKE originates from Coulomb repulsion of the outgoing fragments at a scission configuration) are also shown for comparison. There are two very prominent peaks in the TDHF results around the initial masses of the reactants, with almost no kinetic energy loss, which can be interpreted as the results of (quasi)elastic scattering at peripheral collisions. At small TKE, which corresponds to more central collisions, we note that TKE remains around 340 MeV for all three energies over a wide mass range. This value is about 30 MeV above the Viola systematics, which reflects the properties of deep-inelastic collisions. Moreover, the mass distribution gets wider with increasing incident energy. Shown in Fig. 2(b) is TKE versus scattering angle in c.m. frame ($\theta_{c.m.}$). When TKE is around 340 MeV, $\theta_{c.m.}$ spreads over a very wide range, which also shows deep-inelastic characteristics. For $b = 6$ fm at $E_{c.m.} = 800$ MeV, $\theta_{c.m.} \approx -20°$, is observed which is a result of the strong competition of nuclear attraction, Coulomb repulsion and the centrifugal effect. In the grazing regions, $\theta_{c.m.}$ is almost constant around 85°, 60° and 30° for $E_{c.m.}$=470, 550 and 800 MeV, respectively.

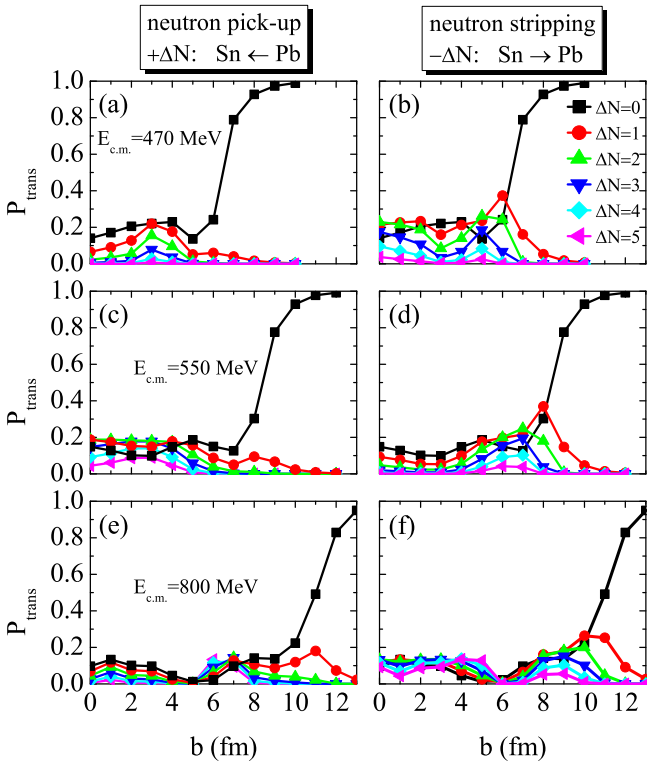

Fig. 3. (color online) Probabilities of neutron pick-up (from the target to the projectile, left panels) and neutron stripping (from the projectile to the target, right panels) channels as functions of the impact parameter for ^{132}Sn + ^{208}Pb at $E_{c.m.}$ = 470 MeV (top panels), 550 MeV (middle panels) and 800 MeV (bottom panels).

The probabilities for different nucleon transfer channels at each impact parameter are obtained from the TDHF final wave functions by using the PNP method. The results of neutron pick-up (from the target to the projectile) and stripping (from the projectile to the target) channels are shown in Fig. 3, while those of the proton pick-up and stripping channels are presented in Fig. 4. Some gross features which can be seen from Figs. 3 and 4 are that the probabilities of $\Delta N = 0$ or $\Delta Z = 0$ increase with increasing impact parameter in the semi-peripheral to peripheral regions. The nucleon transfer process is much reduced in peripheral collisions for all the energies. This is because in peripheral regions, the projectile and target collide gently and the interacting time is not long enough for multi-nucleon exchange. In more central collisions, the probabilities show a complicated dependence on the impact parameter and incident energy.

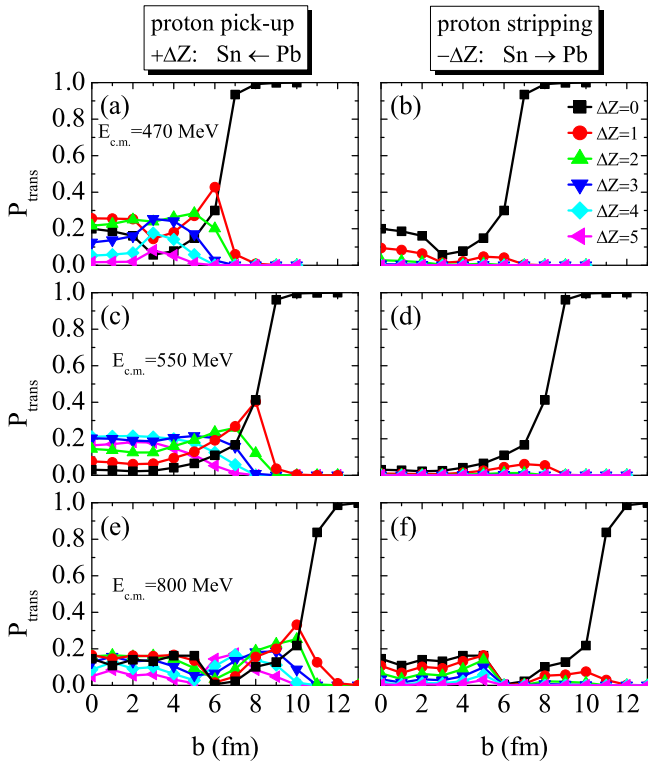

Fig. 4. (color online) Probabilities of proton pick-up (from the target to the projectile, left panels) and proton stripping (from the projectile to the target, right panels) channels as functions of the impact parameter for ^{132}Sn + ^{208}Pb at $E_{\rm c.m.} = 470$ MeV (top panels), 550 MeV (middle panels) and 800 MeV (bottom panels).

To get a clearer insight, the differences between the probabilities of neutron stripping ($-\Delta N$) and pick-up ($+\Delta N$) channels (denoted as $P_{-\Delta N} - P_{+\Delta N}$) are shown in Fig. 5. At $E_{\rm c.m.} = 470$ MeV, the probabilities of neutron stripping channels are larger than those of the pick-up channels for all impact parameters except for $b = 3$ fm. At $E_{\rm c.m.} = 550$ MeV, the probabilities of neutron stripping channels are smaller than those of the pick-up channels for $b \leqslant 4$ fm and larger for $b \geqslant 5$ fm. The probabilities of the neutron stripping channels are found to be larger than those of the pick-up channels for all impact parameters except for $b = 6$ and 7 fm at $E_{\rm c.m.} = 800$ MeV. Though neutron pick-up dominates at certain impact parameters (generally in central and semi-central regions), the total production cross sections for neutron stripping channels are still larger than those for neutron pick-up channels because large impact parameter has larger contributions to the total cross sections, as seen from Eq. (3). The above results indicate that neutron transfer from the projectile to the target is favored.

The differences between the probabilities of proton stripping ($-\Delta Z$) and pick-up ($+\Delta Z$) channels (denoted as $P_{-\Delta Z} - P_{+\Delta Z}$) are shown in Fig. 6. Proton transfer from the target to the projectile is favored for almost all cases. Such nucleon transfer modes are quite beneficial for producing neutron-rich nuclei.

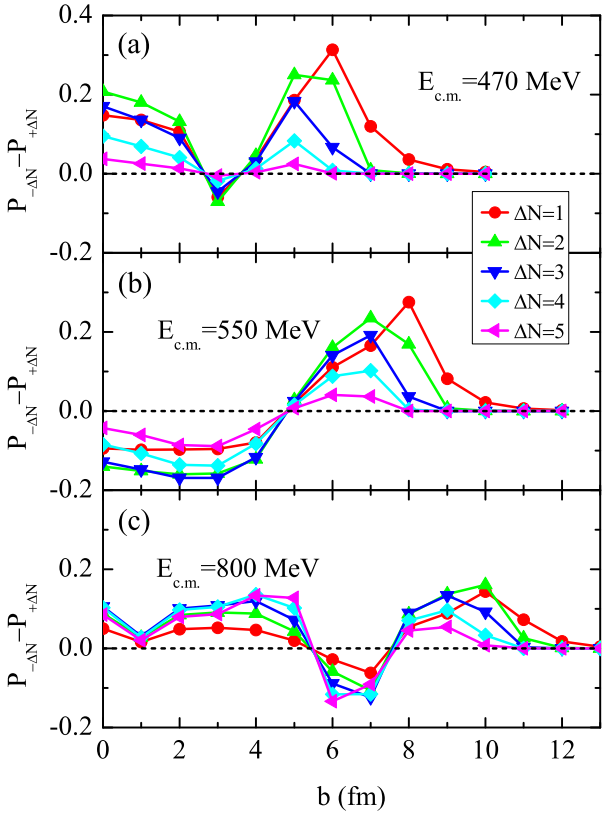

Fig. 5. (color online) Differences between the probabilities of neutron stripping ($-\Delta N$) and pick-up ($+\Delta N$) channels as functions of the impact parameter for ^{132}Sn + ^{208}Pb at $E_{\rm c.m.} = 470$ MeV (top), 550 MeV (middle) and 800 MeV (bottom).

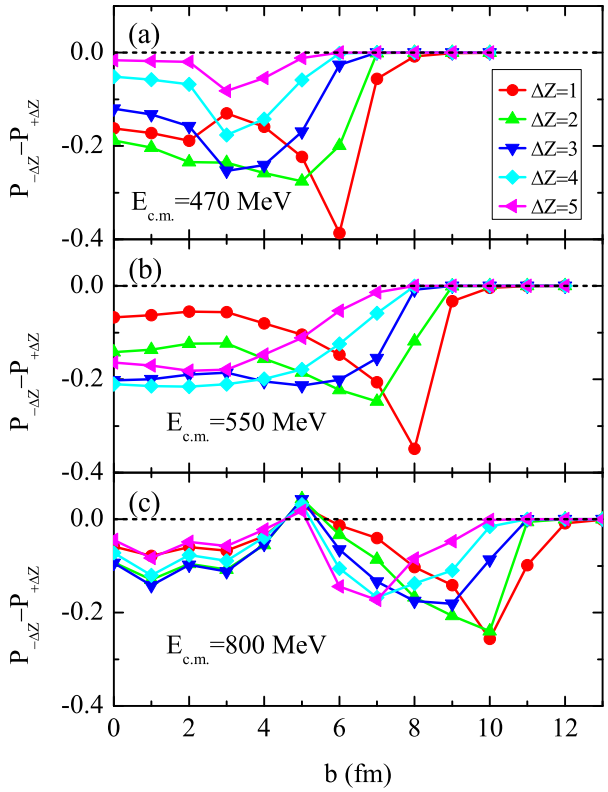

Fig. 6. (color online) Differences between the probabilities of proton stripping ($-\Delta N$) and pick-up ($+\Delta N$) channels as functions of the impact parameter for ^{132}Sn + ^{208}Pb at $E_{\rm c.m.}=470$ MeV (top), 550 MeV (middle) and 800 MeV (bottom).

3.2 Primary and final production cross sections

In this subsection, the production cross sections of the primary TLFs obtained in THDF and those of the final states after deexcitation are calculated by Eqs. (3) and (4).

Shown in Fig. 7 are the isotopic production cross sections of different proton-transfer channels from $Z=77$ to $Z=87$. One can find that for each channel, the primary isotopes are distributed in a broader range than the final isotopes. The primary isotopic distributions also get broader with increasing incident energy. The largest cross sections for isotopes with $Z<82$ depend weakly on the incident energy. For isotopes with $Z>82$, however, their largest cross sections show strong dependence on the incident energy. For example, the largest cross section of francium at $E_{\rm c.m.}=800$ MeV is larger than those of the two lower-energy cases by 2 to 3 orders of magnitude.

After de-excitation, prominent differences between the primary and final results can be found. Firstly, one can see that the distributions for all channels move toward lower N. Exotic nuclei with large isospin asymmetry cannot survive in the de-excitation process. This can be interpreted as the results of neutron evaporation in the de-excitation process. Secondly, prominent decreases for the peak values of the final cross sections are observed for $Z\geqslant 79$, especially for higher incident energies.

To get a deeper insight into these results, the decay modes of a primary fragment with (N,Z) are divided into three types: neutron evaporation (no fission and without light charged particle emission, denoted as mode 1), light charged particle emission (accompanied by neutron evaporation but without fission, denoted as mode 2) and fission of heavy nuclei (accompanied by neutron evaporation and light charged particle emission, denoted as mode 3). The numbers of events for each binary decay mode in GEMINI++ are counted and denoted as $M_{\rm mode\ i}$, where $i=1,2,3$. The relative ratios of these modes are calculated by $\eta_i=\frac{\sigma_{\rm mode\ i}}{\sigma_Z}\times 100\%$, where

$$\sigma_{\rm mode\ i}=2\pi\sum_N\int_{b_{\rm min}}^{b_{\rm max}} b{\rm d}bP_{N,Z}(b)\frac{M_{\rm mode\ i}}{M_{\rm trial}}$$

and $\sigma_Z=\sum_N\sigma_{N,Z}$.

The results for $Z=77$ and 87 are shown as examples. At $E_{\rm c.m.}=470$ MeV, $\eta_1=99.88\%$, $\eta_2=0.1\%$ and $\eta_3=0.02\%$ are obtained for $Z=77$, while the values are 70%, 0.8% and 29.2% for $Z=87$. At $E_{\rm c.m.}=550$ MeV, the contributions are about 87.3%, 12.3% and 0.4% for $Z=77$, while 10.4%, 11.9% and 77.7% for $Z=87$. At $E_{\rm c.m.}=800$ MeV, the contributions are about 16.7%, 75.9% and 7.4% for $Z=77$, while 0%, 27.8% and 72.2% for $Z=87$. Thus we can conclude that fission decay plays an important role in the de-excitation of proton stripping channels.

In Fig. 7(e), (j) and (k), peaks around $N=126$ are seen. This is the result of the quantum effect of the $N=126$ closed neutron shell. The final production cross sections of neutron-rich isotopes show weak dependence on the incident energy. In contrast, those of neutron-deficient isotopes depend strongly on the incident energy. This phenomenon was also observed in Ref. [13].

The production cross sections of neutron-rich heavy nuclei with $N=126$ are extracted from Fig. 7 and plotted in Fig. 8. Both the primary and final cross sections are given.

From Fig. 8 it can be found that both the primary and final products are distributed in a broad range with a peak centered at $Z=82$. From the above discussion of Figs. 3 and 4, it is clear that ^{208}Pb nuclei are mainly from peripheral collisions which correspond to (quasi)elastic scattering. The excitation energies of these fragments are small (seen from Fig. 1) and most of them can survive in the de-excitation process. So both the primary and final cross sections of ^{208}Pb are mainly attributed to (quasi)elastic channels. Note that these cross sections depend on $b_{\rm max}$ (in this work $b_{\rm max}$=10, 12 and 13 fm

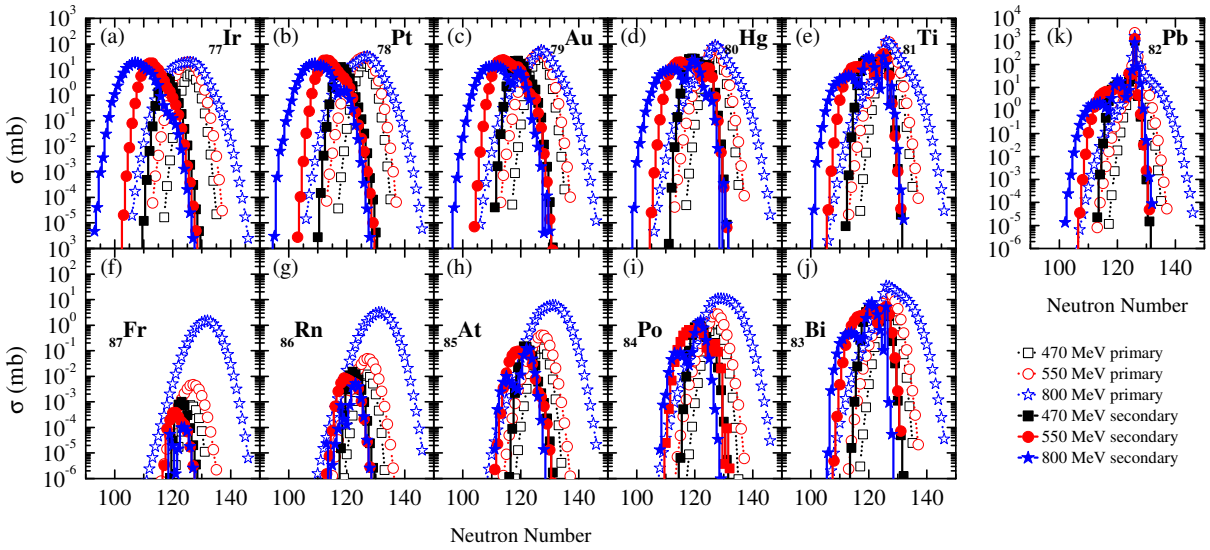

Fig. 7. (color online) Primary (empty symbols with dashed lines) and final (solid symbols with solid histograms) production cross sections of the TLFs for ^{132}Sn + ^{208}Pb at $E_{\rm c.m.}$=470 MeV (black squares), 550 MeV (red circles) and 800 MeV (blue stars).

are used for $E_{\rm c.m.}$=470, 550 and 800 MeV, respectively; as we mentioned at the end of Section 2.1, $b_{\rm max}$ should be large enough to make sure that the transfer cross sections barely depend on it). Unfortunately, it is very hard to separate the total cross sections into components of "(quasi)elastic scattering" or "transfer channels" which makes the cross sections of ^{208}Pb less meaningful. This problem is also found for ^{208}Pb in Fig. 7(k). However, this does not change the conclusions of the present work.

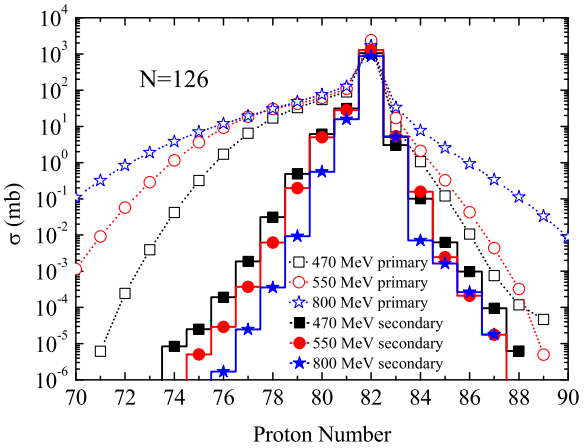

Fig. 8. (color online) Primary (empty symbols with dashed lines) and final (solid symbols with solid histograms) isotonic production cross sections of the nuclei with N=126 for ^{132}Sn + ^{208}Pb at $E_{\rm c.m.}$=470 MeV (black squares), 550 MeV (red circles) and 800 MeV (blue stars).

The primary production cross sections increase with the incident energy, especially for large $|\Delta Z|$ regions. For example, at $E_{\rm c.m.}$ = 800 MeV, the cross sections for $Z = 71$ are orders of magnitude larger than those of the two lower energies. This is because more nucleons are exchanged as the incident energy increases. After de-excitation, however, the production cross sections decrease rapidly as $|\Delta Z|$ increases. Meanwhile, they decrease with increasing incident energy, especially for the lower-Z regions. The cross sections at 800 MeV are at least one order of magnitude lower than those at 470 MeV. This is because much higher excitation energies are involved at $E_{\rm c.m.}$ = 800 MeV and most of those nuclei decay in the de-excitation process.

4 Summary

We have applied the 3D TDHF approach with the PNP method to the MNT reaction ^{132}Sn + ^{208}Pb at various incident energies above the Coulomb barrier. The collision dynamics show the characteristics of deep-inelastic collisions. The impact parameter dependence of the probabilities for different transfer channels indicates that neutron stripping and proton pick-up are favored. Such transfer modes benefit the production of neutron-rich nuclei for the TLF. The production cross sections of the primary fragments depend strongly on the incident energy.

The de-excitation of the primary fragments formed in TDHF were treated by using the state-of-art statistical code GEMINI++. The final isotopic production cross sections of the TLF from $Z = 77$ to $Z = 87$ were investigated. The results reveal that the fission decay of heavy nuclei plays an important role for proton stripping channels. The shell effect is found to be important

in de-excitation for few-nucleon-transfer channels. The production cross sections of neutron-rich nuclei show a slight dependence on the incident energy, even at energies up to 2 times the Bass barrier. The results for neutron-deficient nuclei, however, depend strongly on the incident energy, and much larger cross sections of neutron-deficient nuclei are obtained at higher energies. Finally, the production cross sections of neutron-rich nuclei with $N=126$ are calculated. They decrease gradually as the incident energy increases, especially for lower-Z isotones. This is due to larger excitation energies being involved in higher-energy collisions.

This work presents a self-consistent method to predict yields of neutron-rich nuclei in MNT transfer reactions. However, due to the lack of nucleon-nucleon correlations, mean-field models cannot describe large fluctuations well and the widths of distributions are underestimated. As a first step, the pairing effect can be included in the TDHF approach for transfer reactions. Relevant work is in progress.

References

1 H. Grawe, K. Langanke, and G. Martínez-Pinedo, Rep. Prog. Phys., **70**(9): 1525 (2007)
2 E. M. Kozulin et al, Phys. Rev. C, **86**: 044611 (2012)
3 Y. X. Watanabe et al, Phys. Rev. Lett., **115**: 172503 (2015)
4 V. I. Zagrebaev and W. Greiner, J. Phys. G: Nucl. Part. Phys., **34**(11): 2265 (2007)
5 V. I. Zagrebaev and W. Greiner, Phys. Rev. Lett., **101**: 122701 (2008)
6 V. I. Zagrebaev and W. Greiner, Phys. Rev. C, **83**: 044618 (2011)
7 L. Zhu, J. Su, W.-J. Xie, and F.-S. Zhang, Phys. Lett. B, **767**: 437–442 (2017)
8 C. Li et al, Phys. Lett. B, **776**: 278–283 (2018)
9 O. Beliuskina et al, Eur. Phys. J. A, **50**(10): 161 (2014)
10 J. S. Barrett et al, Phys. Rev. C, **91**: 064615 (2015)
11 A. Winther, Nucl. Phys. A, **572**(1): 191–235 (1994)
12 `http://nrv.jinr.ru/nrv/webnrv/grazing/`
13 Z.-Q. Feng, Phys. Rev. C, **95**: 024615 (2017)
14 L. Zhu, F.-S. Zhang, P.-W. Wen, J. Su, and W.-J. Xie, Phys. Rev. C, **96**: 024606 (2017)
15 N. Wang and L. Guo, Phys. Lett. B, **760**: 236–241 (2016)
16 C. Li, F. Zhang, J.-J. Li, L. Zhu, J.-L. Tian, N. Wang, and F.-S. Zhang, Phys. Rev. C, **93**: 014618 (2016)
17 H. Yao and N. Wang, Phys. Rev. C, **95**: 014607 (2017)
18 M. Bender, P.-H. Heenen, and P.-G. Reinhard, Rev. Mod. Phys., **75**: 121–180 (2003)
19 P. A. M. Dirac, Math. Proc. Cambridge, **26**: 376–385 (1930)
20 C. Simenel and Ph. Chomaz, Phys. Rev. C, **68**: 024302 (2003)
21 T. Nakatsukasa and K. Yabana, Phys. Rev. C, **71**: 024301 (2005)
22 A. S. Umar and V. E. Oberacker, Phys. Rev. C, **71**: 034314 (2005)
23 J. A. Maruhn, P. G. Reinhard, P. D. Stevenson, J. Rikovska Stone, and M. R. Strayer, Phys. Rev. C, **71**: 064328 (2005)
24 A. S. Umar and V. E. Oberacker, Eur. Phys. J. A, **39**: 243–247 (2009)
25 C. Simenel, R. Keser, A. S. Umar, and V. E. Oberacker, Phys. Rev. C, **88**: 024617 (2013)
26 X. Jiang, J. A. Maruhn, and S.-W. Yan, Phys. Rev. C, **90**: 064618 (2014)
27 X. Jiang, J. A. Maruhn, and S. W. Yan, EPL (Europhysics Letters), **112**(1): 12001 (2015)
28 A S Umar, V E Oberacker, J A Maruhn, and P-G Reinhard, J. Phys. G: Nucl. Part. Phys., **37**(6): 064037 (2010)
29 P. Goddard, P. Stevenson, and A. Rios, Phys. Rev. C, **92**: 054610 (2015)
30 C. Simenel and A. S. Umar, Phys. Rev. C, **89**: 031601 (2014)
31 J. A. Maruhn, P.-G. Reinhard, P. D. Stevenson, and M. R. Strayer, Phys. Rev. C, **74**: 027601 (2006)
32 N. Loebl, A. S. Umar, J. A. Maruhn, P.-G. Reinhard, P. D. Stevenson, and V. E. Oberacker, Phys. Rev. C, **86**: 024608 (2012)
33 G.-F. Dai, L. Guo, E.-G. Zhao, and S.-G. Zhou, Phys. Rev. C, **90**: 044609 (2014)
34 G.-F. Dai, L. Guo, E.-G. Zhao, and S.-G. Zhou, Sci. China-Phys. Mech. Astron., **57**(9): 1618–1622 (2014)
35 C. Yu and L. Guo, Sci. China-Phys. Mech. Astron., **60**(9): 092011 (2017)
36 L. Guo, C. Simenel, L. Shi, and C. Yu, Phys. Lett. B, **782**: 401–405 (2018)
37 K. Wen, M. C. Barton, A. Rios, and P. D. Stevenson, Phys. Rev. C, **98**: 014603 (2018)
38 A. S. Umar, C. Simenel, and W. Ye, Phys. Rev. C, **96**: 024625 (2017)
39 C. Simenel, Phys. Rev. Lett., **105**: 192701 (2010)
40 K. Sekizawa, Phys. Rev. C, **96**: 014615 (2017)
41 K. Sekizawa, Phys. Rev. C, **96**: 041601 (2017)
42 X. Jiang and S.-W. Yan, Phys. Rev. C, **90**: 024612 (2014)
43 J. W. Negele, Rev. Mod. Phys., **54**: 913–1015 (1982)
44 R.J. Charity et al, Nucl. Phys. A, **483**(2): 371–405 (1988)
45 W. Hauser and H. Feshbach, Phys. Rev., **87**: 366–373 (1952)
46 R. J. Charity, Joint ICTP-AIEA Advanced Workshop on Model Codes for Spallation Reactions, Report INDC(NDC)-0530 (IAEA), 139 (2008)
47 R. J. Charity, Phys. Rev. C, **82**: 014610 (2010)
48 D. Mancusi, R. J. Charity, and J. Cugnon, Phys. Rev. C, **82**: 044610 (2010)
49 J. A. Maruhn, P.-G. Reinhard, P. D. Stevenson, and A. S. Umar, Comput. Phys. Commun., **185**(7): 2195 – 2216 (2014)
50 E. Chabanat, P. Bonche, P. Haensel, J. Meyer, and R. Schaeffer, Nucl. Phys. A, **635**: 231–256 (1998)
51 P.-G. Reinhard and R.Y. Cusson, Nucl. Phys. A, **378**(3): 418–442 (1982)
52 K. T. R. Davies, H. Flocard, S. Krieger, and M. S. Weiss, Nucl. Phys. A, **342**(1): 111–123 (1980)
53 W. J. Huang, G. Audi, M. Wang, F. G. Kondev, S. Naimi, and X. Xu, Chin. Phys. C, **41**(3): 030002 (2017)
54 M. Wang, G. Audi, F. G. Kondev, W. J. Huang, S. Naimi, and X. Xu, Chin. Phys. C, **41**(3): 030003 (2017)
55 P. Möller, A.J. Sierk, T. Ichikawa, and H. Sagawa, At. Data Nucl. Data Tables, **109-110**: 1–204 (2016)
56 V. E. Viola, K. Kwiatkowski, and M. Walker, Phys. Rev. C, **31**: 1550–1552 (1985)
57 D. J. Hinde, D. Hilscher, H. Rossner, B. Gebauer, M. Lehmann, and M. Wilpert, Phys. Rev. C, **45**: 1229–1259 (1992)